

# Modeling fluid flow and compaction in sedimentary basins using mixed finite elements

Evgeny Kikinzon · Yuri Kuznetsov ·  
Serguei Maliassov · Prasad Sumant

Received: 2 June 2014 / Accepted: 26 January 2015  
© Springer International Publishing Switzerland 2015

**Abstract** In this paper, we present an algorithm and its implementation that was used to numerically study the processes of compaction and fluid flow in a sedimentary basin represented by a two-dimensional model. The model assumes fluid flow to be single phase and compaction to be strictly vertical. On each time step, we use splitting by physical processes to discretize the model equations on a quadrilateral mesh. The movement of the mesh is governed by the laws of the mass and momentum conservation of the sediments, and the fluid flow is resolved using the mixed finite element method on a resulting mesh. Development of geological pinchouts during the simulation is supported. The results of a numerical simulation are presented to verify the implementation of the proposed algorithm.

**Keywords** Basin modeling · Mixed finite elements · Splitting by physical processes · Moving quadrilateral meshes · Geological pinchouts

**Mathematics Subject Classification (2010)** 35Q35 · 74Fxx · 76S05 · 86Axx

## 1 Introduction

In this paper, we consider the process of the sedimentation of a geological basin, which typically has a time span of 10 to 200 million years. A geological basin is a region where sediments are deposited on top of it, with a layer of water above it provided there is no erosion. The underlying porous media, which are filled with water, are compacted because of the increasing pressure. If the permeability of sediments is such that the rate of the water flow is smaller than the deposition rate, there might be an increase in the pore pressure resulting in a lesser degree of compaction. In practice, it is a complicated process involving many lithologies with different rates of deposition and erosion, which is affected by both chemical and mechanical compaction, tectonic forces, erosional and intrusive events, and sea-level changes. We only consider a pure sedimentation process along a 2D profile.

This paper presents the description of the algorithm and its implementation which are used to model the processes of compaction and fluid flow in a sedimentary basin. We assume the basin to be two-dimensional, fluid flow to be single phase, and compaction to be strictly vertical. The model used in this paper can also be found in [4], with similar model equations previously discussed in [1, 15–17], and

---

This work is a part of research projects supported in 2011–2012 by ExxonMobil Upstream Research Company, Houston, TX.

---

E. Kikinzon (✉) · Y. Kuznetsov  
Department of Mathematics, University of Houston,  
651 PGH, Houston, TX 77204, USA  
e-mail: kikinzon@math.uh.edu

Y. Kuznetsov  
e-mail: kuz@math.uh.edu

S. Maliassov · P. Sumant  
ExxonMobil Upstream Research Company, 3120 Buffalo  
Speedway, Houston, TX 77098, USA

S. Maliassov  
e-mail: serguei.maliassov@exxonmobil.com

P. Sumant  
e-mail: prasad.sumant@exxonmobil.com

[18]. The purpose of this article is to propose an algorithm that enables the numerical simulation of that model on an expanding quadrilateral mesh and utilizes the finite element discretizations.

Numerical simulation of the formation of sedimentary basins allows to estimate the pressure and permeability history, which enables better understanding of how hydrocarbons were migrating and accumulating over time. Finite element methods, which provide higher accuracy when computing pressures and velocities compared to difference methods, such as finite volume method, thus become an important tool for obtaining reliable results. It is particularly true for non-rectangular meshes typical for geological basins due to their irregular geometry, which often includes declining sediment layers and barriers of different permeabilities.

Our algorithm is based on splitting of the sedimentation process into sequential processes of compaction and fluid flow. The resolution of the mesh on every time step is based on the discrete laws of the conservation of the mass and momentum of the sediments. It is followed by solving the fluid flow problem, which is discretized using the mixed hybrid finite element method [3, 12]. This approach allows us to model basins with many lithologies, including the cases of geological pinchouts.

The notable works in this area that use a different approach can be found in [6]. Coupling of geomechanics and fluid flow is also studied in the context of the reservoir simulation and hydraulic fracturing [13, 14]. The work in that area includes error estimates and results on convergence (see [2, 10, 11, 19]).

The paper is organized as follows. In Section 2, we describe the equations used to model the sedimentation process and present the full system of non-linear equations governing the model. In Section 3, we provide the general framework of the algorithm we employ to numerically simulate the sedimentation process according to the given system of differential equations. This algorithm is based on the idea of splitting the global physical process into deposition, compaction, and fluid flow stages. In Section 4, we give the description of the quadrilateral mesh of a particular structure that is used to represent the geometry of the basin throughout the simulation. In Section 5, we discretize the model equations from Section 2 on the mesh given in Section 4. The discrete equation is written in a way that allows us to use them in the framework of the algorithm given in Section 3. In Section 6, we provide the details on a particular implementation of the algorithm from Section 3. Explicit description of the procedures used to carry out every step of the algorithm is given. In Section 7, we present the results of a numerical simulation that uses the implementation of the algorithm given in Section 6.

## 2 Model equations

We describe the processes of compaction and fluid flow in a sedimentary basin by a system of coupled non-linear equations. We assume the basin to be two-dimensional, fluid flow to be single phase, and compaction to be strictly vertical.

An example of the computational domain  $\Omega$  is given in Fig. 1. The  $z$ -axis is associated with the depth and is directed from the top to the bottom of the basin. We assume  $z_{\text{top}}(t)$ , the top boundary of  $\Omega$ , to be known at all times  $t$ .

For any given volume  $V \in \Omega$ , we introduce two densities:

- $\rho_s$ : density of the solid rock
- $\rho_a$ : density of the fluid

We assume that the rock is incompressible, i.e., that  $\rho_s \equiv \text{const}$ , and that the fluid is compressible with its density governed by the equation

$$\rho_a(p) = \rho_0 e^{\alpha(p-p_{\text{atm}})}, \quad (1)$$

where  $p$  is the pore pressure,  $\alpha$  is a compressibility coefficient for water, and  $p_{\text{atm}}$  is the atmospheric pressure.

We assume that between every two moments of time  $t$ , a certain amount of porous rock filled with water is deposited on top of the basin. We denote the amount of the solid rock in the deposit by  $q_s = q_s(x, t)$  and assume that the initial porosity of the deposit is  $\phi_{\text{dep}} = \phi_{\text{dep}}(x, t)$ .

The first law governing the sedimentation process is the *conservation of the solid mass*. Due to the assumption that the compaction is strictly vertical, the conservation law can

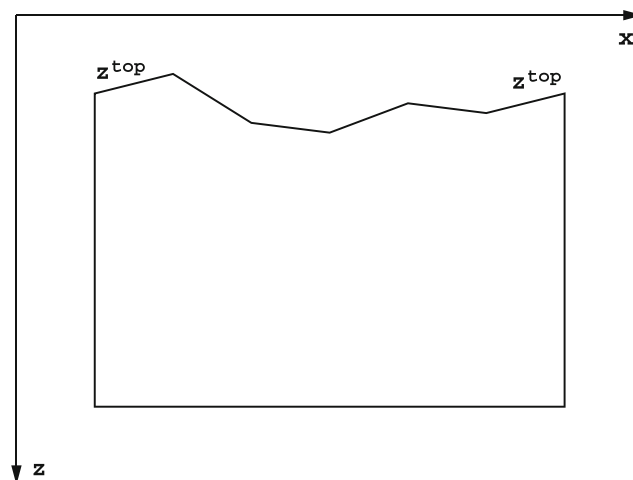


Fig. 1 An example of the domain

be written in the following form:

$$\int_{z_{\text{top}}^t(x)}^{z^t} \rho_s (1 - \phi^t(x)) dz = \int_{z_{\text{top}}^\tau(x)}^{z^\tau} \rho_s (1 - \phi^\tau(x)) dz + \int_{\tau}^t q_s(x, r) dr, \quad (2)$$

where  $\tau < t$ ,  $z^t$  is the position of the point  $z^\tau$  at time  $t$  and  $\phi^t(x)$  is the porosity of the rock between points  $z_{\text{top}}^\tau(x)$  and  $z^\tau$  at time  $t$ .

We only consider the case of  $q_s(t) \geq 0$ , i.e., the deposition of the rock, and ignore the process of erosion.

Although the top boundary of  $\Omega$  is known at all times, the bottom boundary is determined by the sedimentation process and changes over time as the depth of the basin increases.

The second law is the law describing the *change of the porosity of the solid rock*, which is as follows:

$$\phi = \phi_0 e^{-\beta(\sigma - p)}, \quad (3)$$

where  $\phi_0$  and  $\beta$  are known constants for a given type of material and  $\sigma$  is the vertical stress or the bulk pressure due to the weight of the sediments and the water above.

It is governed by the third law, which is the *conservation of the momentum for the solid rock*. The full stress is a tensor that can be written as

$$\sigma_{\text{full}} = \begin{pmatrix} \sigma_x & \sigma_{xz} \\ \sigma_{zx} & \sigma_z \end{pmatrix}, \quad (4)$$

but due to the assumptions that the compaction is strictly vertical and that  $\sigma_{zx} \equiv 0$ , we have to consider only one component of  $\sigma_{\text{full}}$ , namely we set  $\sigma \equiv \sigma_z$ , the vertical stress, for which we can write

$$\frac{\partial \sigma}{\partial z} = (\rho_s(1 - \phi) + \rho_a(p)\phi) g \quad (5)$$

with the boundary conditions

$$\sigma(z_{\text{top}}^t) \equiv \sigma_{\text{top}}^t \equiv p_{\text{top}}^t \quad \text{for all } t. \quad (6)$$

Here,  $p_{\text{top}}$  is defined as

$$p_{\text{top}} = \begin{cases} p_{\text{atm}} + \rho_a(p_{\text{atm}})gz_{\text{top}}, & z_{\text{top}} \geq 0, \\ p_{\text{atm}}, & \text{otherwise.} \end{cases} \quad (7)$$

In the integral form, the law can be written as

$$\sigma(x, z) = \sigma_{\text{top}}(x) + \int_{z_{\text{top}}(x)}^z (\rho_s(1 - \phi(x)) + \rho_a(p)\phi(x)) g dz. \quad (8)$$

The fourth and the last law is the *conservation of the fluid mass* given by

$$\frac{\partial (\rho_a(p)\phi)}{\partial t} + \nabla \cdot (\rho_a(p)\phi u_w) = q_a(x, t), \quad (9)$$

where  $u_w$  is the total velocity of water, and  $q_a(x, t)$  is the amount of the fluid in the deposit, that is

$$q_a(x, t) = \frac{\phi_{\text{dep}} \rho_a(p)}{(1 - \phi_{\text{dep}}) \rho_s} q_s(x, t). \quad (10)$$

We define the Darcy velocity, i.e., the water flux relative to the solid rock, as

$$u = \phi(u_w - u_s) = -\frac{1}{\mu} K(\phi) (\nabla p - \rho_a(p)g). \quad (11)$$

Here,  $u_s$  is the velocity of the solid rock, i.e., the component of the flux associated with the movement of the domain,  $\mu$  is the viscosity of the fluid,  $K(\phi)$  is the permeability, and  $g$  is the gravity vector.

For our model, we use the Koseny-Carman equation modified for the case of porosities less than 10 %,

$$K(\phi) = k(\phi)K_0, \quad (12)$$

where

$$K_0 = k_0 \begin{pmatrix} 1 & 0 \\ 0 & k_z \end{pmatrix} \quad (13)$$

and

$$k(\phi) = \begin{cases} \frac{\phi^3}{(1 - \phi)^2}, & \phi \geq 0.1, \\ 100 \frac{\phi^5}{(1 - \phi)^2}, & \phi < 0.1. \end{cases} \quad (14)$$

Here,  $k_0$  and  $k_z$  are constants describing the physical properties of the rock.

We complement these equations by the Dirichlet type conditions on the top boundary,

$$p|_{z_{\text{top}}} \equiv p_{\text{top}} \equiv \sigma_{\text{top}}, \quad (15)$$

and homogeneous Neumann conditions on the remaining part of the boundary,  $\Gamma_N \equiv \partial\Omega \setminus \Gamma_D$ ,

$$u \cdot n|_{\Gamma_N} \equiv 0. \quad (16)$$

As the result, we obtain the system of non-linear equations used to model the sedimentation process.

### 3 Splitting by physical processes

Let us give a general description of the splitting algorithm used to solve the non-linear system of equations presented in Section 2.

That system is fully coupled, in particular, the geometry of the domain  $\Omega$  depends on the pore pressure through the change of the porosity. If we use the mesh  $\Omega_h$  and discretize the equations describing the fluid flow by an MFE method, matrices in the resulting algebraic formulation will depend on the mesh and, therefore, the domain geometry.

To be able to obtain explicit Jacobians for the non-linear system, we therefore need to decouple the changes in mesh

geometry and pore pressure. We do that by using the splitting of the sedimentation process into consecutive processes of compaction and fluid flow.

Moreover, we should add new cells to the mesh  $\Omega_h$  as additional rock is deposited and the depth of the basin increases. Therefore, the deposition process has to be separated from the compaction and the fluid flow processes and resolved first. Consequently, the non-linear systems for compaction and fluid flow will no longer include deposition terms.

Let us consider a time interval between times  $t_k$  and  $t_{k+1}$  and assume that an amount  $q_s^{k+1}(x)$  of solid rock filled with the amount  $q_a^{k+1}(x)$  of water is deposited during that time. The top boundary of the basin at time  $t_{k+1}$  is known to be  $z_{\text{top}}^{k+1}(x)$ .

Let the mesh  $\Omega_h^k$  and the values of parameters  $p^k$ ,  $\phi^k$ , and  $\sigma^k$  at time  $t_k$  be known, then in order to obtain their values at time  $t_{k+1}$ , we use the following algorithm.

**Step 1: deposition.** Based on the initial mesh  $\Omega_h^k$ , the given amount of deposits  $q_s^{k+1}(x)$ , their porosity, and the known top boundary  $z_{\text{top}}^{k+1}(x)$ , we obtain the post-deposition mesh  $\widehat{\Omega}_h$ . This mesh has the entire amount of the deposit for the current time interval added on top. If that resulted in creation of new cells, initial guess values of the parameters  $\widehat{p}$ ,  $\widehat{\phi}$ , and  $\widehat{\sigma}$  for these cells are also determined. For other cells, these values might be kept from the previous time interval.

Note that the creation of new mesh cells is the reason why the deposition has to be resolved separately.

Another important point is that the amount of solid rock in a cell can only change during this step.

**Step 2: compaction.** Under the assumption that the change in pore pressure during the considered time interval is sufficiently small, we set  $p \equiv \widehat{p} \equiv \text{const}$  and solve the system of non-linear equations governing the compaction process (namely, Eqs. 2, 3, and 8 in Section 2) on the mesh  $\widehat{\Omega}_h$ , that is,

$$\begin{aligned} \int_{z_{\text{top}}^{k+1}(x)}^{z^{k+1}} \rho_s (1 - \phi^{k+1}(x)) dz &= \int_{\widehat{z}_{\text{top}}(x)}^{\widehat{z}} \rho_s (1 - \widehat{\phi}(x)) dz, \\ \phi^{k+1} &= \phi_0 e^{-\beta(\sigma^{k+1} - \widehat{p})}, \\ \sigma^{k+1}(x, z) &= \sigma_{\text{top}}^{k+1} \\ &+ \int_{z_{\text{top}}^{k+1}(x)}^{z^{k+1}} \left( \rho_s (1 - \phi^{k+1}(x)) + \rho_a(\widehat{p}) \phi^{k+1}(x) \right) g dz, \end{aligned} \quad (17)$$

to obtain the new values of parameters  $\phi$  and  $\sigma$ , which we set to be their values at time  $t_{k+1}$ ,  $\phi^{k+1}$ , and  $\sigma^{k+1}$ . We also obtain the post-compaction mesh, which we set to be  $\Omega_h^{k+1}$ .

Note that we assume the porosity  $\phi$  for every cell to be non-increasing and set  $\phi^{k+1} = \phi^k$ , recomputing other parameters as well, if this condition is violated.

Another important point is that unlike in Eq. 2, the term with  $q_s^{k+1}(x)$  is not present because the deposition of the solid rock is already resolved on the deposition step.

**Step 3: fluid flow.** Under the assumption that the change in pore pressure is sufficiently small, we set the post-compaction mesh geometry, as well as the corresponding values of porosity and stress parameters, to be constant, i.e., we assume that after the compaction step, we have already obtained their values at time  $t_{k+1}$  and solve the system of non-linear equations governing the fluid flow process (namely Eqs. 9, 11, 15, and 16 in Section 2) on the fixed mesh  $\Omega_h^{k+1}$ , that is, we solve

$$\begin{aligned} \frac{\partial (\rho_a(p^{k+1})\phi^{k+1})}{\partial t} + \nabla \cdot (\rho_a(p^{k+1})\phi^{k+1}u_w^{k+1}) &= 0, \\ u^{k+1} &= \phi^{k+1} (u_w^{k+1} - u_s^{k+1}) \\ &= -\frac{1}{\mu} K(\phi^{k+1}) (\nabla p^{k+1} - \rho_a(p^{k+1})g), \\ p^{k+1}|_{\Gamma_D} &\equiv p_{\text{top}}^{k+1}, \\ u^{k+1} \cdot n^{k+1}|_{\Gamma_N} &\equiv 0 \end{aligned} \quad (18)$$

to obtain the new value of the parameter  $p$  at time  $t_{k+1}$ ,  $p^{k+1}$ .

Using this algorithm, we find the new values  $\phi^{k+1}$  and  $\sigma^{k+1}$ , as well as the mesh  $\Omega_h^{k+1}$ , after resolving the compaction process and determine the new value of the last parameter,  $p^{k+1}$ , after resolving the fluid flow process.

Note that unlike in Eq. 9, the term with  $q_a^{k+1}(x)$  is not present because on the deposition step, the new material is already added in the uncompressed state with the pores filled with water.

Another important point is that every time we assume the mesh geometry,  $\Omega_h$ , not to change, we should also assume that the porosity,  $\phi$ , does not change either. If the area of a mesh cell remains the same, but the porosity for that cell changes, it corresponds to the change in the solid mass in that mesh cell. During the compaction and the fluid flow steps, we impose the conservation of the solid mass law on each mesh cell, so any changes in the solid mass in a cell would imply that the law is violated in that mesh cell.

Due to the use of splitting, the change in geometry and the change in pore pressure do not occur simultaneously. In fact, the mesh  $\Omega_h^{k+1}$ , as well as the values of parameters  $\phi^{k+1}$  and  $\sigma^{k+1}$ , correspond to the post-deposition values of the pore pressure,  $\widehat{p}$ , while the final post-fluid flow values,  $p^{k+1}$ , are generally different. Therefore, the computed values of  $\phi^{k+1}$ ,  $\sigma^{k+1}$ , and  $p^{k+1}$  will not satisfy the change of porosity law (3) exactly.

To ensure that this error is sufficiently small, on every time interval  $[t_k, t_{k+1}]$ , once the deposition step has been

performed, we can repeat the compaction and fluid flow steps several times in order to obtain a value of the pore pressure  $\hat{p}$  that does not significantly change over these steps, i.e., the values of  $\hat{p}$  and  $p^{k+1}$  match up to a chosen level of accuracy.

The procedure is as follows:

Let  $\tilde{\Omega}$  be the post-deposition basin with the corresponding initial value of the pore pressure  $\hat{p}$ .

*Correction step:* For a copy of the basin  $\tilde{\Omega} \equiv \hat{\Omega}$ :

1. Set  $\tilde{p}^k = \hat{p}$ .
2. Make the compaction step.
3. Make the fluid flow step.
4. Set  $\tilde{p} = \tilde{p}^{k+1}$ .

Let the the relative change in pore pressure over the correction step,  $\delta_{\tilde{p}}$ , be defined by

$$\delta_{\tilde{p}} = \frac{\|\tilde{p}^{k+1} - \tilde{p}^k\|}{\|\tilde{p}^k\|}. \quad (19)$$

Then, we should repeat the correction step until  $\delta_{\tilde{p}}$  becomes sufficiently small for the change of porosity law to be satisfied with the required precision.

#### 4 Mesh description

We assume the problem mesh  $\Omega_h$  to be a conforming quadrilateral mesh with the following structure. Let  $\{x_i\}_{i=1}^{n_{\text{col}}+1}$  be a grid used to partition the domain  $\Omega$  with respect to the  $x$ -coordinate. We assume that all the cells are quadrilaterals, and two faces of every cell are strictly vertical, i.e., they lie on two adjacent lines  $x = x_i$  and  $x = x_{i+1}$  for a certain  $i$ .

This implies that for a given  $\{x_i\}_{i=1}^{n_{\text{col}}+1}$ , the mesh  $\Omega_h$  can be represented as a union of  $n_{\text{col}}$  vertically adjacent strips of cells, which we call *mesh columns*, and denote by  $C_i$ ,  $i = \overline{1, n_{\text{col}}}$ .

We denote mesh cells by  $e_{i,j}$ , where  $i$  denotes the mesh column and  $j$  denotes the position in the corresponding mesh column, indexing is done from the bottom to the top.

We require all mesh columns to contain the same number of cells,  $n_{\text{row}}$ , at any given moment of time. Therefore, the mesh  $\Omega_h$  can also be represented as a union of  $n_{\text{row}}$  horizontally adjacent strips of cells, which we call *mesh rows*, and denote by  $R_j$ ,  $j = \overline{1, n_{\text{row}}}$ .

This allows us to represent the structure of the mesh by mesh columns,  $\Omega_h = \bigcup_{i=1}^{n_{\text{col}}} C_i$ , where  $C_i = \bigcup_{j=1}^{n_{\text{row}}} e_{i,j}$ , or by mesh rows,  $\Omega_h = \bigcup_{j=1}^{n_{\text{row}}} R_j$ , where  $R_j = \bigcup_{i=1}^{n_{\text{col}}} e_{i,j}$ .

Mesh nodes are indexed in a similar way. All mesh cells are quadrilaterals, so a mesh cell  $e_{i,j}$  has bottom-left node  $z_{i,j}$ , bottom-right node  $z_{i+1,j}$ , top-right node  $z_{i+1,j+1}$ , and top-left node  $z_{i,j+1}$ .

An illustration of the mesh structure is given in Fig. 2.

We associate a parameter  $\epsilon_0$  with the mesh  $\Omega_h$ . This parameter determines the minimal distance between two mesh nodes and, consequently, the minimal length of a cell's face.

We call faces of length  $\epsilon_0$  degenerate, and we call cells with two degenerate faces empty. Note that due to the structure of the mesh, only vertical faces can be degenerate.

Therefore, while all the cells are quadrilateral and all the mesh columns contain  $n_{\text{row}}$  cells, given sufficiently small  $\epsilon_0$ , such mesh can be used to approximate geometries with triangular cells and mesh columns containing different number of cells, which makes it suitable for simulations of basins with geological pinchouts.

Note that on the fluid flow step, a special version of this mesh is used. We obtain it by eliminating all the empty cells and all the degenerate faces. This results in a mesh with quadrilateral and triangular cells, where every face has the length greater than  $\epsilon_0$ .

#### 5 Discrete equations

Now we can discretize the model equations from Section 2 on the mesh  $\Omega_h$  described in Section 4.

We assume the values of the parameters  $p$ ,  $\phi$ , and  $\sigma$  to be constant inside of each mesh cell  $E_{i,j} \in \Omega_h$  and associate these cell-average values with the geometrical center of the cell denoted by  $z_{c,i,j}$ .

According to the splitting algorithm, deposition of the additional rock is handled separately from compaction and fluid flow processes. Given a certain moment of time  $t_k$ , we consider the basin  $\hat{\Omega}$ , for which we assume the deposition to be already resolved, and write the discrete equations used to determine its state at the following time moment  $t_{k+1}$ , namely the geometry of the mesh  $\Omega_h^{k+1}$  and parameters  $p^{k+1}$ ,  $\phi^{k+1}$ , and  $\sigma^{k+1}$ .

For every cell  $E \in \Omega_h$ , we denote its post-deposition state by  $\hat{E}$  with corresponding volume denoted by  $|\hat{E}|$  and values of other parameters denoted by  $\hat{p}$ ,  $\hat{\phi}$ , and  $\hat{\sigma}$ .

##### 5.1 Discrete conservation of the solid mass law

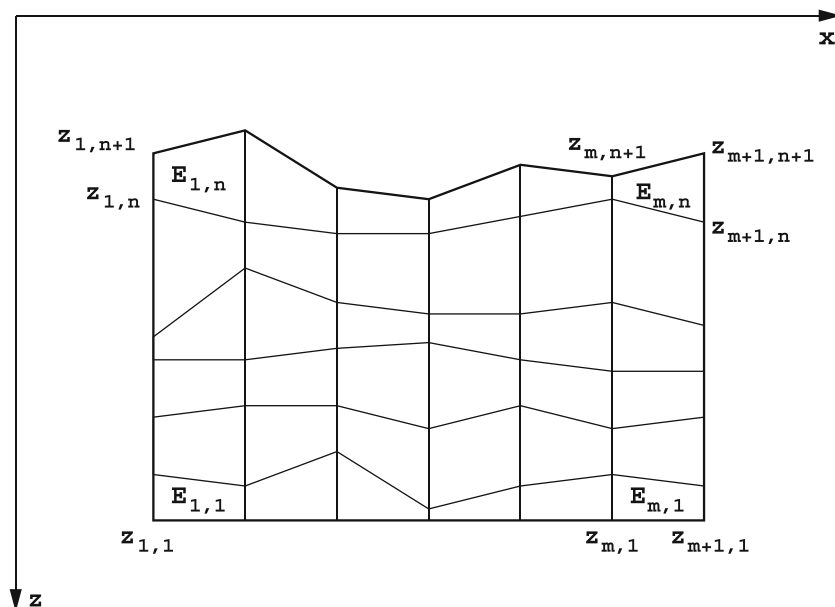
For every mesh cell  $E_{i,j} \in \Omega_h$ , once the deposition is resolved, the conservation of the solid mass law can be written as

$$\int_{E_{i,j}^{k+1}} \rho_s (1 - \phi_{i,j}^{k+1}) dx = \int_{\hat{E}_{i,j}} \rho_s (1 - \hat{\phi}_{i,j}) dx. \quad (20)$$

With porosity being constant inside a cell, the law for a single cell  $E_{i,j}$  is as follows:

$$(1 - \phi_{i,j}^{k+1}) |E_{i,j}^{k+1}| = (1 - \hat{\phi}_{i,j}) |\hat{E}_{i,j}|. \quad (21)$$

**Fig. 2** An illustration of the mesh structure. Here,  $m$  stands for  $n_{\text{col}}$ , and  $n$  stands for  $n_{\text{row}}$



## 5.2 Discrete change of the porosity law

Values of parameters  $p$ ,  $\phi$ , and  $\sigma$  are assumed to be constant inside a cell, so the change of the porosity law for a cell  $E_{i,j}$  can be written as

$$\phi_{i,j}^{k+1} = \phi_0 e^{-\beta(\sigma_{i,j}^{k+1} - p_{i,j}^{k+1})}. \quad (22)$$

In the splitting algorithm, though, it is implied that the change in porosity and the change in pressure are resolved separately. Therefore, the new values of  $\phi$  and  $\sigma$  are found for a current value of  $p$  which is assumed to be constant. Hence, the discretization used in the implementation of the algorithm is as follows:

$$\phi_{i,j}^{k+1} = \phi_0 e^{-\beta(\sigma_{i,j}^{k+1} - \hat{p}_{i,j})}. \quad (23)$$

## 5.3 Discrete conservation of the momentum law

Let  $z_{\text{top},i,j}$  be the center of the top face of a cell  $E_{i,j}$ ,

$$z_{\text{top},i,j} = \frac{1}{2} (z_{i,j+1} + z_{i+1,j+1}), \quad (24)$$

then the discrete conservation of the momentum law can be written as

$$\begin{aligned} \sigma_{i,j}^{k+1} &= \sigma_{\text{top},i,j}^{k+1} \\ &+ \int_{z_{\text{top},i,j}^{k+1}}^{z_{c,i,j}^{k+1}} \left( \rho_s (1 - \phi_{i,j}^{k+1}) + \rho_a (p_{i,j}^{k+1}) \phi_{i,j}^{k+1} \right) g \, dx, \end{aligned} \quad (25)$$

where  $\sigma_{\text{top},i,j}^{k+1} \equiv \sigma^{k+1}|_{z_{\text{top},i,j}^{k+1}}$ .

With values of parameters  $p$ ,  $\phi$ , and  $\sigma$  being constant inside the cells, we have

$$\begin{aligned} &\int_{z_{c,i,j}^{k+1}}^{z_{\text{top},i,j}^{k+1}} \left( \rho_s (1 - \phi_{i,j+1}^{k+1}) + \rho_a (p_{i,j+1}^{k+1}) \phi_{i,j+1}^{k+1} \right) g \, dx = \\ &\int_{z_{c,i,j}^{k+1}}^{z_{\text{top},i,j}^{k+1}} \left( \rho_s (1 - \phi_{i,j+1}^{k+1}) + \rho_a (p_{i,j+1}^{k+1}) \phi_{i,j+1}^{k+1} \right) g \, dx, \end{aligned} \quad (26)$$

and the parameter  $\sigma$  is associated with the center of  $E_{i,j+1}$ , i.e.,  $\sigma_{i,j+1}^{k+1} \equiv \sigma^{k+1}|_{z_{c,i,j+1}^{k+1}}$ ; therefore,

$$\sigma_{i,j+1}^{k+1} - \sigma_{\text{top},i,j+1}^{k+1} = \sigma_{\text{top},i,j}^{k+1} - \sigma_{i,j+1}^{k+1}. \quad (27)$$

Hence, we can write

$$\sigma_{\text{top},i,j}^{k+1} = \begin{cases} p_{\text{top},i}^{k+1}, & j = n_{\text{row}}, \\ 2\sigma_{i,j+1}^{k+1} - \sigma_{\text{top},i,j+1}^{k+1}, & j < n_{\text{row}}, \end{cases} \quad (28)$$

where  $p_{\text{top},i}^{k+1}$  is the pressure at the top of mesh column  $C_i^{k+1}$ ,

$$z_{\text{top},i}^{k+1} = z_{\text{top}}^{k+1} \left( \frac{x_i + x_{i+1}}{2} \right), \quad (29)$$

found using Eq. 7.

In the implementation of the algorithm, where  $p$  is fixed, the following discrete law is used:

$$\begin{aligned} \sigma_{i,j}^{k+1} &= \sigma_{\text{top},i,j}^{k+1} \\ &+ \left( \rho_s (1 - \phi_{i,j}^{k+1}) + \rho_a (\hat{p}_{i,j}) \phi_{i,j}^{k+1} \right) g \left( z_{c,i,j}^{k+1} - z_{\text{top},i,j}^{k+1} \right). \end{aligned} \quad (30)$$



Note that

$$z_{\text{top},i,j}^{k+1} = \begin{cases} z_{\text{top},i}^{k+1}, & j = n_{\text{row}}, \\ 2z_{c,i,j+1}^{k+1} - z_{\text{top},i,j+1}^{k+1}, & j < n_{\text{row}}. \end{cases} \quad (31)$$

Therefore, the only geometrical variables in the discrete conservation of the momentum law are the centers of the cells.

#### 5.4 Discrete conservation of the fluid mass law

To discretize equations in Eq. 18, we use mixed finite elements method. Let  $P_h \in L_2(\Omega)$  and  $V_h \in H_{\text{div}}(\Omega)$  be finite dimensional subspaces such that for any  $q \in P_h$  and  $v \in V_h$ , the following holds:

$$\begin{aligned} q &\equiv \text{const} && \text{in every cell } E_{i,j}. \\ \nabla \cdot v &\equiv \text{const} && \text{in every cell } E_{i,j}. \end{aligned} \quad (32)$$

$$v \cdot n_{k,l} \equiv \text{const} \text{ on every face } \Gamma_{k,l}.$$

By the general transport theorem, for any cell  $E_{i,j} \in \Omega_h$ , we have

$$\int_{E_{i,j}} \frac{\partial (\rho_a(p)\phi)}{\partial t} dx = \frac{d}{dt} \int_{E_{i,j}} \rho_a(p)\phi dx - \int_{E_{i,j}} \nabla \cdot (\rho_a(p)\phi u_s) dx. \quad (33)$$

Assuming that no water is being deposited into  $E_{i,j}$ , we can write the conservation of the fluid mass law (9) for this cell as

$$\frac{d}{dt} \int_{E_{i,j}} \rho_a(p)\phi dx + \int_{E_{i,j}} \nabla \cdot (\rho_a(p)\phi u) dx = 0, \quad (34)$$

where  $u$  is the Darcy velocity defined in Eq. 11.

Therefore, for the conservation of the fluid mass law to hold in every cell  $E_{i,j}$  on the fluid flow step, i.e., when the deposition has already been resolved, we have to find functions  $p \in P_h$  and  $u \in V_h$  such that

$$\frac{d}{dt} \int_{E_{i,j}} \rho_a(p_{i,j})\phi_{i,j}q_{i,j} dx + \int_{E_{i,j}} \nabla \cdot (\rho_a(p_{i,j})u_{i,j})q_{i,j} dx = 0 \quad (35)$$

for any  $q \in P_h$ . Here,  $p_{i,j} = p|_{E_{i,j}}$  and  $u_{i,j} = u|_{E_{i,j}}$ .

Additionally, functions  $p$  and  $u$  should satisfy the Darcy's law in every cell  $E_{i,j}$ :

$$\begin{aligned} &\int_{E_{i,j}} \left( \mu K_{i,j}^{-1}(\phi_{i,j})u_{i,j} \right) \cdot v_{i,j} dx \\ &+ \int_{E_{i,j}} (\nabla p_{i,j} - \rho_a(p_{i,j})g) \cdot v_{i,j} dx = 0 \end{aligned} \quad (36)$$

or

$$\begin{aligned} &\int_{E_{i,j}} \left( \mu K_{i,j}^{-1}(\phi_{i,j})u_{i,j} \right) \cdot v_{i,j} dx - \int_{E_{i,j}} p_{i,j} (\nabla \cdot v_{i,j}) dx + \\ &+ \int_{\partial E_{i,j}} p_{i,j} (v_{i,j} \cdot n) ds - \int_{E_{i,j}} \rho_a(p_{i,j}) (g \cdot v_{i,j}) dx = 0 \end{aligned} \quad (37)$$

for any  $v \in V_h$ ,  $v_{i,j} = v|_{E_{i,j}}$ .

Let  $M_{K,i,j}$  and  $M_{I,i,j}$  be mass matrices such that

$$(M_{K,i,j}\bar{u}_{i,j}, \bar{v}_{i,j}) = \int_{E_{i,j}} \left( K_{i,j}^{-1}(\phi_{i,j})u_{i,j} \right) \cdot v_{i,j} dx \quad (38)$$

and

$$(M_{I,i,j}\bar{u}_{i,j}, \bar{v}_{i,j}) = \int_{E_{i,j}} u_{i,j} \cdot v_{i,j} dx. \quad (39)$$

Then, the algebraic form of the Eq. 37 is as follows:

$$\begin{aligned} &\mu M_{K,i,j}\bar{u}_{i,j} + B_{i,j}^T p_{i,j} + C_{i,j}^T \bar{\lambda}_{i,j} \\ &- \rho_a(p_{i,j})M_{I,i,j}\bar{g}_{n,i,j} = 0, \end{aligned} \quad (40)$$

where  $B_{i,j}$  and  $C_{i,j}$  are standard matrices used in local mixed hybrid finite element discretization. If a cell  $E_{i,j}$  has faces  $\Gamma_{i,j,s}$ ,  $s = \overline{1, n_{\Gamma,i,j}}$ , then the components of the vector  $\bar{g}_{n,i,j}$  are defined by

$$\begin{aligned} g_{n,i,j,s} &= \frac{1}{|\Gamma_{i,j,s}|} \int_{\Gamma_{i,j,s}} g_{i,j} \cdot n_{i,j,s} ds = g_{i,j} \cdot n_{i,j,s}, \\ s &= \overline{1, n_{\Gamma,i,j}}. \end{aligned} \quad (41)$$

We can now express the flux  $\bar{u}_{i,j}$  in terms of  $p_{i,j}$  and  $\lambda_{i,j}$ :

$$\begin{aligned} \bar{u}_{i,j} &= -\frac{1}{\mu} M_{K0,i,j}^{-1} \left( B_{i,j}^T p_{i,j} + C_{i,j}^T \bar{\lambda}_{i,j} \right. \\ &\left. - \rho_a(p_{i,j})M_{I,i,j}\bar{g}_{n,i,j} \right). \end{aligned} \quad (42)$$

To obtain the discrete conservation of the fluid mass law, we first use the implicit finite difference method to discretize Eq. 35 with respect to time:

$$\begin{aligned} &(t_{k+1} - t_k) \int_{E_{i,j}^{k+1}} \nabla \cdot \left( \rho_a(p_{i,j}^{k+1})u_{i,j}^{k+1} \right) q_{i,j} dx \\ &+ \int_{E_{i,j}^{k+1}} \rho_a(p_{i,j}^{k+1})\phi_{i,j}^{k+1}q_{i,j} dx - \int_{\hat{E}_{i,j}} \rho_a(\hat{p}_{i,j})\hat{\phi}_{i,j}q_{i,j} dx = 0. \end{aligned} \quad (43)$$

Therefore, the discrete conservation of the fluid mass law can be written as

$$\begin{aligned} &-B_{i,j}^{k+1}\bar{u}_{i,j}^{k+1} \\ &+ \frac{1}{t_{k+1} - t_k} \left( \phi_{i,j}^{k+1}|E_{i,j}^{k+1}| - \frac{\rho_a(\hat{p}_{i,j})}{\rho_a(p_{i,j}^{k+1})}\hat{\phi}_{i,j}|\hat{E}_{i,j}| \right) = 0 \end{aligned} \quad (44)$$

where

$$\begin{aligned} \bar{u}_{i,j}^{k+1} = & -\frac{1}{\mu} \left( M_{K,i,j}^{k+1} \right)^{-1} \left( \left( B_{i,j}^{k+1} \right)^T p_{i,j}^{k+1} + \right. \\ & \left. + \left( C_{i,j}^{k+1} \right)^T \bar{\lambda}_{i,j}^{k+1} - \rho_a (p_{i,j}^{k+1}) M_{I,i,j}^{k+1} \bar{g}_{n,i,j}^{k+1} \right). \end{aligned} \quad (45)$$

The interface and the Neumann boundary conditions can be written as

$$C_{i,j}^{k+1} \bar{u}_{i,j}^{k+1} = 0, \quad (46)$$

and the discrete form of Dirichlet boundary conditions is as follows:

$$\lambda_{i,j,s}^{k+1} = p_{\text{top},i}^{k+1} \quad \text{for } i = \overline{1, n_{\text{col}}} \text{ and } (j, s) \text{ s.t. } \Gamma_{i,j,s} \in \Gamma_D. \quad (47)$$

In general, any mixed finite element method that provides accurate results on meshes with triangular and quadrilateral cells can be used to discretize the conservation of the fluid mass law. For example, while performing the numerical experiments, we compared the PWCF method [8, 9] and the Kuznetsov-Repin (KR) MFE method [7]. The obtained results were nearly identical, so the computational cost became the deciding factor in giving preference to the PWCF method.

## 6 Implementation of the algorithm

In this section, we describe the implementation of the algorithm given in Section 3 which uses the discrete equations derived in Section 5.

We assume that at the starting time  $t_0$  the basin  $\Omega$  is empty, and we are given the partitioning of the mesh  $\Omega_h$  with respect to the  $x$ -coordinate,  $\{x_i\}_{i=1}^{n_{\text{col}}+1}$ , and the value of the minimal face length  $\epsilon_0$ .

Let  $\{t_i\}_{i=0}^{n_t}$  be a sequence of moments in time for which we resolve the state of the basin  $\Omega$ . We assume that during each time interval  $[t_{k-1}, t_k]$ ,  $k = \overline{1, n_t}$ , an associated deposit is added to the top of the basin.

Let  $G_{\text{fin}}$  be the final state of the basin  $\Omega$  that is known. The deposition data required to perform the simulation and obtain  $\Omega^{n_t}$ , the basin at the end of the simulation, is estimated based on  $G_{\text{fin}}$ .

Let  $G_{\text{fin}}^k$  be a bed in  $G_{\text{fin}}$  associated with the rock deposited during the time interval  $[t_{k-1}, t_k]$ , i.e., it is the final state of that deposit. The bed  $G_{\text{fin}}^k$  can be partitioned into columns  $g_{\text{fin},i}^k$  with respect to the grid  $\{x_i\}_{i=1}^{n_{\text{col}}+1}$ ,  $G_{\text{fin}}^k = \bigcup_{i=1}^{n_{\text{col}}} g_{\text{fin},i}^k$ .

Note that the partitioning of  $G_{\text{fin}}$  into  $G_{\text{fin}}^k$  can be performed based on a chosen time sequence  $\{t_i\}_{i=0}^{n_t}$  or a chosen partitioning into  $G_{\text{fin}}^k$  can determine the considered time intervals.

The geometry of  $G_{\text{fin}}$  is known. Therefore, the geometry of its part  $G_{\text{fin}}^k$  is also known. We assume that the material inside each column  $g_{\text{fin},i}^k$  is homogeneous, its porosity is constant, and an estimate for porosity,  $\phi_{\text{fin},i}$ ,  $i = \overline{1, n_{\text{col}}}$ , is given.

The top and the bottom boundary of  $G_{\text{fin}}^k$  are piece-wise linear, and we denote the thickness or the height of  $G_{\text{fin}}^k$  along the lines separating columns  $g_{\text{fin},i}^k$  by  $h_{\text{fin}}^k(x_i)$ .

An example of a bed  $G_{\text{fin}}^k$  is given in Fig. 3.

On each time interval  $[t_{k-1}, t_k]$ , we use the following data to perform the simulation:

- $\{z_{\text{top}}^k(x_i)\}_{i=1}^{n_{\text{col}}+1}$ : piece-wise linear top boundary of the mesh  $\Omega_h$  at  $t = t_k$ ;
- $\{h_{\text{fin}}^k(x_i)\}_{i=1}^{n_{\text{col}}+1}$ : thickness of the corresponding bed  $G_{\text{fin}}^k$ ;
- $\{\phi_{\text{fin},i}^k\}_{i=1}^{n_{\text{col}}}$ : list of porosity estimates for corresponding columns  $g_{\text{fin},i}^k$ ,  $i = \overline{1, n_{\text{col}}}$ ; and
- $\rho_s^k, \phi_0^k, \beta^k, k_0^k$ , and  $k_z^k$ : parameters defining the properties of the rock associated with  $G_{\text{fin}}^k$ .

Provided that  $G_{\text{fin}}$ , the basin in its final state, is observed at  $t = n_t$  and that the simulation data above is estimated accurately, we should obtain  $\Omega^{n_t}$ , the basin at the end of the simulation, which is sufficiently close to  $G_{\text{fin}}$ .

### 6.1 Deposition step

Let us consider the time interval  $[t_k, t_{k+1}]$  with corresponding data for the top boundary  $\{z_{\text{top}}^{k+1}(x_i)\}_{i=1}^{n_{\text{col}}+1}$  and the bed  $G_{\text{fin}}^{k+1}$  with its associated parameters.

First, we reconstruct the deposit  $G^{k+1}$  which corresponds to a bed  $G_{\text{fin}}^{k+1}$ , i.e., based on the final state of the bed  $G_{\text{fin}}^{k+1}$ , we estimate the state of the rock that formed it at the time when it had been deposited. To do so, we have to estimate the original values of deposit's thickness,  $\{h^{k+1}(x_i)\}_{i=1}^{n_{\text{col}}+1}$ , and porosities,  $\{\phi_i^{k+1}\}_{i=1}^{n_{\text{col}}}$ , associated with columns  $g_i^{k+1}$ .

We assume the rock to be uncompressed or almost uncompressed at the time of deposition and obtain the deposit  $G$  such that

- Porosities  $\phi_i$ ,  $i = \overline{1, n_{\text{col}}}$ , are close to  $\phi_0$ .

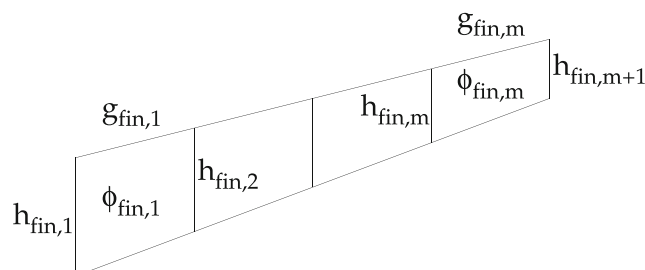


**Fig. 3** An example of a bed  $G_{\text{fin}}^k$  in its final state. Here,  $m$  stands for  $n_{\text{col}}$



- The mass of the solid rock inside a column  $g_i$  is preserved, i.e.,  $\rho_s (1 - \phi_i) S_i = \rho_s (1 - \phi_{\text{fin},i}) S_{\text{fin},i}$ , where  $S$  is the size of  $g_i$ .
- $h_i \geq \epsilon_0$ ,  $i = 1, n_{\text{col}} + 1$ .

An example of the resulting deposit  $G$  is shown in Fig. 4.

There are two cases to consider when adding the deposit  $G^{k+1}$  to the existing mesh  $\Omega_h^k$ :

- If the type of rock in the deposit column  $g_i^{k+1}$  is different from the type of rock in the top cell of the mesh column  $C_i$ ,  $E_{i,n_{\text{row}}}$ , we add new cells on top of  $C_i$  to account for the deposit.
- If the type of rock in the deposit column  $g_i^{k+1}$  is the same as in the top cell of the mesh column  $C_i$ ,  $E_{i,n_{\text{row}}}$ , and the same holds for at least one adjacent mesh column,  $C_{i-1}$  or  $C_{i+1}$ , we first add the deposit to the top cell, expanding its faces on one or both sides up to the desirable thickness.

If the cell  $E_{i,n_{\text{row}}}$  is an “empty” cell, we consider the first non-empty cell from the top in the same mesh column, say,  $E_{i,j}$ . If the materials matching condition is satisfied for  $E_{i,j}$  as well, we add the deposit to  $E_{i,j}$ , then to all the empty cells above it, going from the bottom to the top and expanding the cells up to the desirable thickness as long as there remains some material to be deposited.

If the materials matching condition is not satisfied for the cell  $E_{i,j}$ , we start adding the deposit to an empty cell closest to  $E_{i,j}$  from above for which the condition holds.

If there remains some rock to be deposited after we have finished expanding the existing cells, we start adding new cells on top of  $C_i$ .

Note that when we have to add a new cell on top of any  $C_i$ , we create an entire new mesh row.

The idea behind the described procedure is to create new cells only if the type of the deposited rock changes or if the thickness of at least one of the cells in the top mesh row exceeds the desired value. Because we always create entire new mesh rows, some of the cells in these rows may be empty. In special cases, this can result in several empty cells stacked on top of each other. Then, if possible, we later add deposits to the cell at the bottom of such stack first.

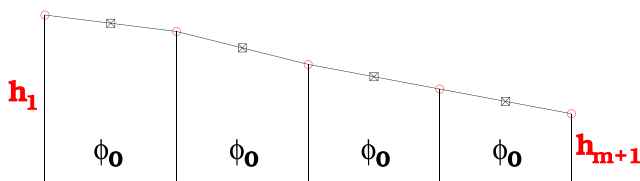


Fig. 4 Reconstructed deposit  $G$  with porosity  $\phi_0$

Following that, all the mesh nodes are shifted so that the top boundary matches the one specified by  $\{z_{\text{top}}^{k+1}(x_i)\}_{i=1}^{n_{\text{col}}+1}$ . This gives us the post-deposition mesh  $\hat{\Omega}_h$ .

For a cell  $\hat{E}_{i,j}$  that did not have any new deposits added to it, i.e., such that  $|\hat{E}_{i,j}| = |E_{i,j}^k|$ , we keep the values of the parameters from the previous time step setting  $\hat{\phi}_{i,j} = \phi_{i,j}^k$ ,  $\hat{\sigma}_{i,j} = \sigma_{i,j}^k$ , and  $\hat{p}_{i,j} = p_{i,j}^k$ . These values are going to be updated during the compaction and the fluid flow steps.

Now, let us consider a cell  $\hat{E}_{i,j} \in \hat{\Omega}_h$  to which some material has been added to.

- If  $\hat{E}_{i,j}$  is a new cell added to the mesh, we set the post-deposition value of the porosity,  $\hat{\phi}_{i,j}$ , to be the same as in the corresponding deposit column  $g_i^{k+1}$ .
- If  $\hat{E}_{i,j}$  was an existing cell and its size has been increased, we set the post-deposition value of the porosity,  $\hat{\phi}_{i,j}$ , to be the volume average of the porosity of the material in  $\hat{E}_{i,j}$  before the deposition,  $\phi_{i,j}^k$ , and the porosity of the material in the corresponding deposit column  $g_i^{k+1}$ , i.e.,

$$\hat{\phi}_{i,j} = \frac{1}{|\hat{E}_{i,j}|} \left( \phi_{i,j}^k |E_{i,j}^k| + \phi_i^{k+1} (|\hat{E}_{i,j}| - |E_{i,j}^k|) \right). \quad (48)$$

Then, for all cells  $\hat{E}_{i,j} \in \hat{\Omega}_h$  such that  $\hat{E}_{i,j}$  is a new cell or  $|\hat{E}_{i,j}| \neq |E_{i,j}^k|$ , we do the following. Let  $\hat{z}_{c,i,j}$  be a center of the cell  $\hat{E}_{i,j}$  as before, then we approximate the post-deposition value of the stress parameter by

$$\hat{\sigma}_{i,j} = \hat{\sigma}_{\text{top},i,j} + (\rho_s (1 - \hat{\phi}_{i,j}) + \rho_a (p_{\text{hs}}(\hat{z}_{c,i,j})) \hat{\phi}_{i,j}) g (\hat{z}_{c,i,j} - \hat{z}_{\text{top},i,j}), \quad (49)$$

where  $p_{\text{hs}}(\hat{z}_{c,i,j})$  is the approximation of the hydrostatic pressure at the center of the cell,

$$p_{\text{hs}}(z) = p_{\text{atm}} + \rho_a (p_{\text{atm}}) g z. \quad (50)$$

The post-deposition value of the pore pressure in the cell  $E_{i,j}$  is then computed according to the change of the porosity law:

$$\hat{p}_{i,j} = \hat{\sigma}_{i,j} + \frac{1}{\beta_{i,j}} \ln \frac{\hat{\phi}_{i,j}}{\phi_0}. \quad (51)$$

Note that by creating new cells and changing the size and the porosity of existing cells  $E_{i,j}$  from  $|E_{i,j}^k|$  to  $|\hat{E}_{i,j}|$  and  $\phi_{i,j}^k$  to  $\hat{\phi}_{i,j}$ , respectively, we completely resolve the addition of  $q_s^{k+1}$  and  $q_a^{k+1}$  to every mesh column  $C_i$ , as per Eq. 2. Consequently, the amount of the solid rock in a cell can only change during the deposition step, while during the compaction and the fluid flow steps, we impose the conservation of the solid mass law on each mesh cell.

The reason for why the deposition process has to be resolved on a separate step is the need to create new mesh

cells. For the proposed algorithm, it is important that we always add new cells as parts of new mesh rows, with some of the cells in new rows possibly empty. We also never mix different types of rock in one mesh cell. The exact implementation of the deposition procedure might differ dependent on the specific requirements, but these two points should be always satisfied.

## 6.2 Compaction step

After the deposition step has been performed and the post-deposition state of the basin has been obtained, we proceed to the compaction step on the time interval  $[t_k, t_{k+1}]$ .

According to our algorithm, the system of discrete equation governing the compaction for a cell  $E_{i,j}$  is as follows:

$$\begin{aligned} (1 - \phi_{i,j}^{k+1}) |E_{i,j}^{k+1}| &= (1 - \widehat{\phi}_{i,j}) |\widehat{E}_{i,j}|, \\ \phi_{i,j}^{k+1} &= \phi_0 e^{-\beta(\sigma_{i,j}^{k+1} - \widehat{p}_{i,j})}, \\ \sigma_{i,j}^{k+1} &= \sigma_{\text{top},i,j}^{k+1} \\ &+ \left( \rho_s (1 - \phi_{i,j}^{k+1}) + \rho_a (\widehat{p}_{i,j}) \phi_{i,j}^{k+1} \right) g \left( z_{c,i,j}^{k+1} - z_{\text{top},i,j}^{k+1} \right) \end{aligned} \quad (52)$$

with the boundary conditions

$$\sigma_{\text{top},i,n_{\text{row}}}^{k+1} = p_{\text{top}}(z_{\text{top},i}^{k+1}). \quad (53)$$

Substituting

$$\phi_{i,j}^{k+1} = \phi_0 e^{-\beta(\sigma_{i,j}^{k+1} - \widehat{p}_{i,j})} \quad (54)$$

and

$$\left( z_{c,i,j}^{k+1} - z_{\text{top},i,j}^{k+1} \right) = \frac{1 - \widehat{\phi}_{i,j}}{1 - \phi_{i,j}^{k+1}} (\widehat{z}_{c,i,j} - \widehat{z}_{\text{top},i,j}) \quad (55)$$

into the discrete conservation of the momentum law, we obtain a scalar non-linear equation in one unknown,

$$f(\sigma_{i,j}^{k+1}) = 0, \quad (56)$$

where

$$\begin{aligned} f(\sigma_{i,j}^{k+1}) &= \sigma_{i,j}^{k+1} - \sigma_{\text{top},i,j}^{k+1} - \left( \rho_s (1 - \phi_0 e^{-\beta(\sigma_{i,j}^{k+1} - \widehat{p}_{i,j})}) + \right. \\ &\quad \left. + \rho_a (\widehat{p}_{i,j}) \phi_0 e^{-\beta(\sigma_{i,j}^{k+1} - \widehat{p}_{i,j})} \right) \frac{(1 - \widehat{\phi}_{i,j}) g (\widehat{z}_{c,i,j} - \widehat{z}_{\text{top},i,j})}{1 - \phi_0 e^{-\beta(\sigma_{i,j}^{k+1} - \widehat{p}_{i,j})}}. \end{aligned} \quad (57)$$

Note that due to the assumption on the compaction being strictly vertical and the consequent assumptions on the stress tensor, the compaction problem for the basin  $\Omega$  breaks into  $n_{\text{col}}$  independent problems for mesh columns  $C_i$ ,  $i = \overline{1, n_{\text{col}}}$ , each of which can be solved cell by cell, going from the top cell  $E_{i,n_{\text{row}}}$  to the bottom cell  $E_{i,1}$ .

Moreover, as shown above, the problem for each mesh cell can be reduced to a scalar non-linear equation in one unknown given in Eq. 56.

Solving the compaction problem, we obtain new coordinates of the centers of the cells,  $z_{c,i,j}^{k+1}$ , and new volumes of the cells,  $|E_{i,j}^{k+1}|$ . To recover the conforming quadrilateral mesh, we perform the mesh reconstruction.

Reconstruction of the mesh and solving the system for compaction are performed together. Note that the top boundary  $\{z_{\text{top}}^{k+1}(x_i)\}_{i=1}^{n_{\text{col}}+1}$  is given; therefore, new coordinates of mesh nodes  $z_{i,n_{\text{row}}+1}$ ,  $i = \overline{1, n_{\text{col}}+1}$  are explicitly known. Hence, going mesh row by mesh row, from the top row  $R_{n_{\text{row}}}$  to the bottom row  $R_1$ , on each mesh row  $R_j$ , we can perform the following procedure:

1. Solve the compaction problem cell by cell for all the cells  $E_{i,j}$  of the mesh row  $R_j$ .
2. For every cell  $E_{i,j}$ ,  $i = \overline{1, n_{\text{col}}}$ , find the new center of the bottom face,  $z_{b,i,j}^{k+1}$ , based on the known new top face,  $\Gamma_{i,j}^{k+1} = (z_{i,j+1}^{k+1}, z_{i+1,j+1}^{k+1})$ , and new center of the cell,  $z_{c,i,j}^{k+1}$ .
3. Choose the  $z$ -coordinate of the node  $z_{1,j}^{k+1}$  and construct a piecewise-linear bottom boundary passing through the node  $z_{1,j}^{k+1}$  and nodes  $z_{b,i,j}^{k+1}$ ,  $i = \overline{1, n_{\text{col}}}$ , to reconstruct the conforming quadrilateral mesh in the mesh row  $R_j$ .

Note that because the mesh  $\Omega_h^{k+1}$  is quadrilateral, this procedure preserves the volume of the cells.

## 6.3 Fluid flow step

Now, we consider the fluid flow step on the time interval  $[t_k, t_{k+1}]$ . We assume that the compaction step has already been performed; therefore, the new state of the mesh,  $\Omega_h^{k+1}$ , as well as the new values of parameters  $\phi_{i,j}^{k+1}$  and  $\sigma_{i,j}^{k+1}$  have been determined for all cells  $E_{i,j}$ .

Following the algorithm, the local system of discrete equation governing the fluid flow in a cell  $E_{i,j}$  can be written in terms of solution vectors  $p_{i,k}^{k+1}$  and  $\bar{\lambda}_{i,j}^{k+1}$ :

$$\begin{aligned} &\frac{1}{\mu} B_{i,j}^{k+1} (M_{K,i,j}^{k+1})^{-1} \left( (B_{i,j}^{k+1})^T p_{i,j}^{k+1} + \right. \\ &\quad \left. + (C_{i,j}^{k+1})^T \bar{\lambda}_{i,j}^{k+1} - \rho_a (p_{i,j}^{k+1}) M_{l,i,j}^{k+1} \bar{g}_{n,i,j}^{k+1} \right) + \\ &\quad + \frac{1}{t_{k+1} - t_k} \left( \phi_{i,j}^{k+1} |E_{i,j}^{k+1}| - \frac{\rho_a (\widehat{p}_{i,j})}{\rho_a (p_{i,j}^{k+1})} \widehat{\phi}_{i,j} |\widehat{E}_{i,j}| \right) = 0, \\ &C_{i,j}^{k+1} (M_{K,i,j}^{k+1})^{-1} \left( (B_{i,j}^{k+1})^T p_{i,j}^{k+1} + \right. \\ &\quad \left. + (C_{i,j}^{k+1})^T \bar{\lambda}_{i,j}^{k+1} - \rho_a (p_{i,j}^{k+1}) M_{l,i,j}^{k+1} \bar{g}_{n,i,j}^{k+1} \right) = 0, \\ &\lambda_{i,j,s}^{k+1} = p_{\text{top},i}^{k+1} \quad \text{if } \Gamma_{i,j,s} \in \Gamma_D. \end{aligned} \quad (58)$$

The global non-linear system in terms of solution vectors  $\bar{p}^{k+1}$  and  $\bar{\lambda}^{k+1}$  can be written as the assembling of local

non-linear systems above. We solve the global system using the Newton's method with initial guess given by the vectors  $\bar{p}^k$  and  $\bar{\lambda}^k$ .

The Jacobian for the global system can be obtained by assembling the Jacobians for the local systems.

We eliminate all empty cells and degenerate faces from the mesh when we discretize the fluid flow system.

## 7 Numerical simulation

Let us illustrate the proposed algorithm by performing a numerical simulation using the implementation of the algorithm described in Section 6.

We use the discretization with piece-wise constant fluxes (PWCF method) [8, 9] in our implementation of the MFE method.

In the implementation of the Newton's method used on the fluid flow step described in Section 6.3, to solve the underlying algebraic system, we use the direct method, namely the UMFPACK algorithm (see [5] for more details).

We use the following values of physical constants for water:

$$\begin{aligned}\mu &= 3 \cdot 10^{-4} \text{ N} \cdot \text{s} \cdot \text{m}^{-2} \\ \rho_0 &= 1030 \text{ kg/m}^3 \\ \alpha &= 4.35 \cdot 10^{-4} \text{ MPa}^{-1}\end{aligned}$$

In our example, we consider the formation of a basin with a pinchout layer which contains two types of rock. The first type of rock is deposited over two time intervals [0, 10] Ma and [15, 20] Ma. The second type, which forms the pinchout layer, is deposited over the time interval [10, 15] Ma.

The basin is partitioned into 20 mesh columns, and time step is chosen to be 1 Ma, i.e., for the purpose of providing the deposition data, the final geometry is uniformly partitioned into 20 beds.

An illustration of the desired basin geometry at the final time is given in Fig. 5. Note that this final geometry usually corresponds to the currently observed state of a basin. Together with the estimates for the final values of the porosity, it is used to determine the provided simulation data such as the amount and the type of past deposits. If the final geometry corresponds to some later times after the end of deposition and the simulation does not include "relaxation" time interval with no deposition at the end, then the geometry at the end of the simulation can be different from the final geometry. It can also differ if the estimates for the final values of the porosity were inaccurate, thus serving as a tool to verify them.

In this example, we only consider the time period when the active deposition had been occurring, i.e., the end of the simulation corresponds to the end of the deposition.

The physical properties of the rock deposited over time intervals [0, 10] Ma and [15, 20] Ma are described by the following constants:

$$\begin{aligned}\rho_s &= 2500 \text{ kg/m}^3, \quad \phi_0 = 0.25 \\ k_0 &= 9 \text{ mD}, \quad k_z = 0.1 \\ \beta &= 0.04 \text{ MPa}^{-1}\end{aligned}$$

The physical properties of the second type of rock deposited over the time interval [10, 15] Ma are given by:

$$\begin{aligned}\rho_s &= 2800 \text{ kg/m}^3, \quad \phi_0 = 0.4 \\ k_0 &= 562.5 \text{ mD}, \quad k_z = 1 \\ \beta &= 0.025 \text{ MPa}^{-1}\end{aligned}$$

We use a coarser mesh and a finer mesh: The finer mesh has twice as many mesh cells in the vertical direction, i.e., the number of mesh rows is doubled.

On each time interval, we perform the correction steps until  $\delta \tilde{p}$ , as defined in Eq. 19, satisfies  $\delta \tilde{p} < 0.001$ . On the coarser mesh, satisfying that condition takes from 4 to 41 iterations of the compaction and the fluid flow steps per time interval, for a total of 287 iterations over the entire simulation. On the finer mesh, it takes from 4 to 31 iterations

**Fig. 5** Target basin geometry for numerical simulation

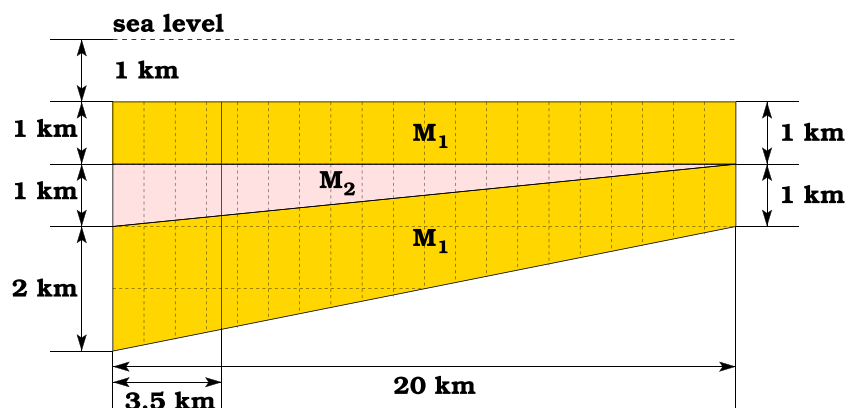


**Fig. 6** Pressure distribution at  $t = 20$  Ma for the coarser mesh

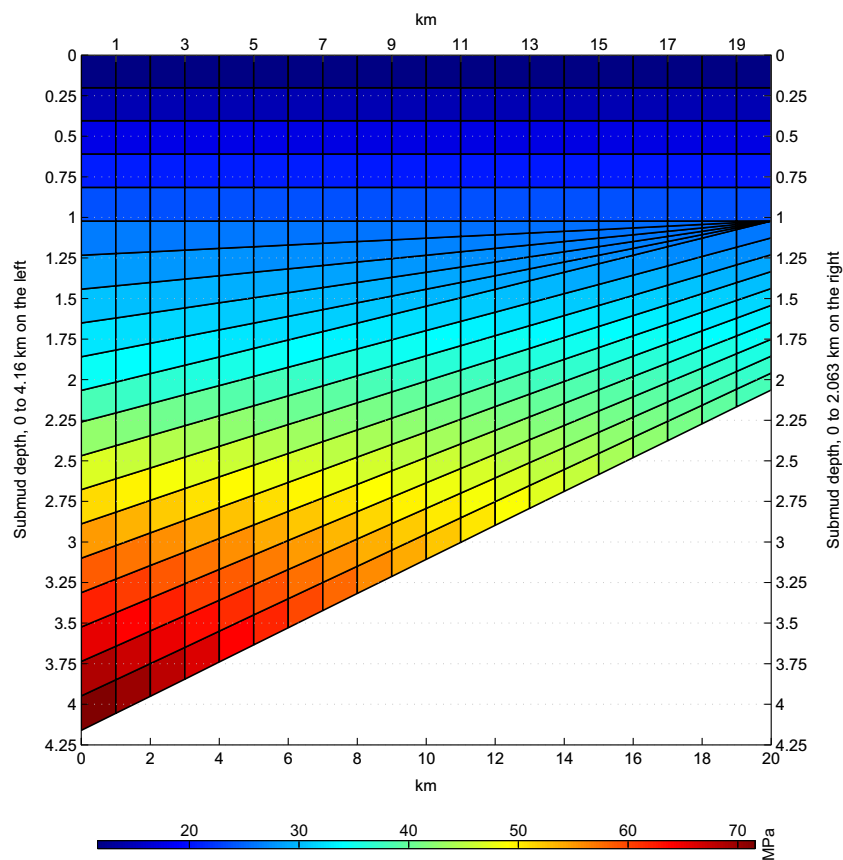
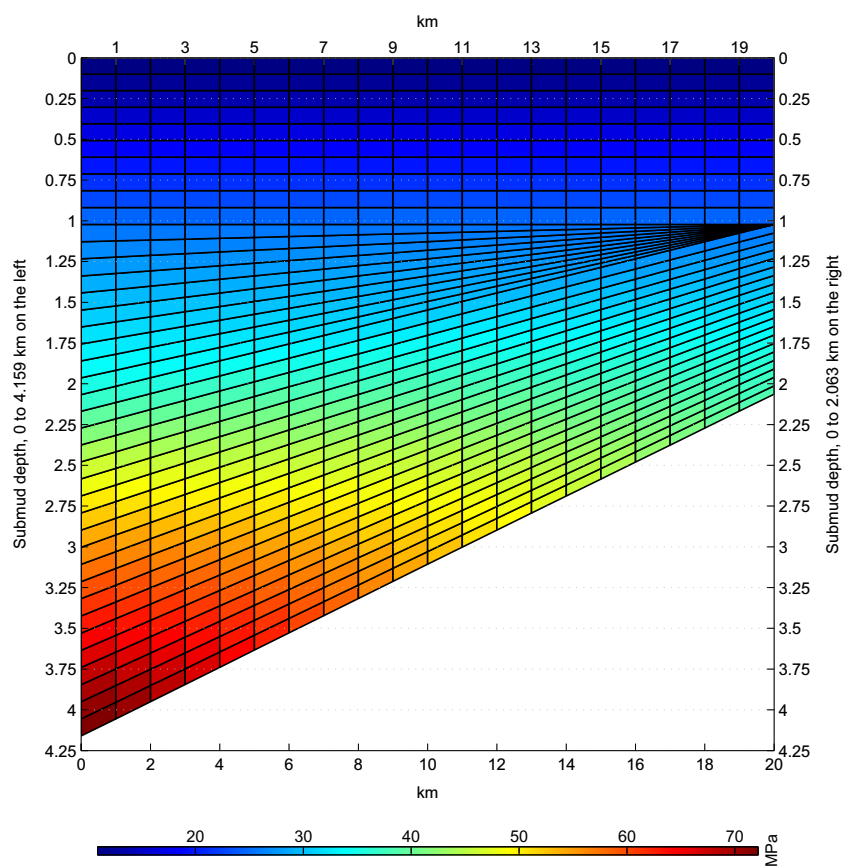


**Fig. 7** Pressure distribution at  $t = 20$  Ma for the finer mesh



per time interval for a total of 283 iterations over the entire simulation.

The geometry of the basin at the end of the simulation is shown in Fig. 6 for the coarser mesh and in Fig. 7 for the finer mesh.

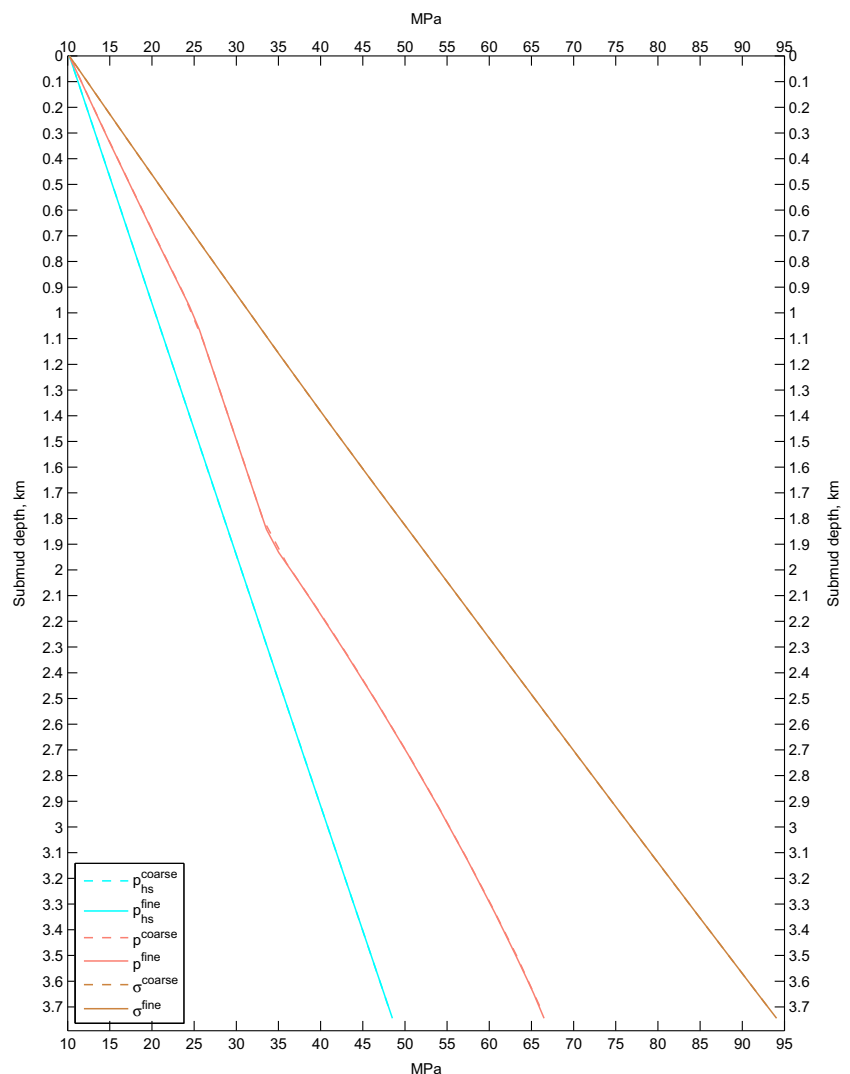
The computed values of pressures (hydrostatic pressure  $p_{hs}$ , pore pressure  $p$ , stress or bulk pressure  $\sigma$ ) and porosities along the fourth mesh column are given in Figs. 8 and 9, respectively. This corresponds to values along the vertical line  $x = 3.5$  km which passes through the centers of the cells in the fourth mesh column and is marked in red in Fig. 5. For the ease of comparison, we plot the results on the coarser and on the finer meshes on the same figures.

This example serves as an illustration of the point made in Section 1: If, due to the low permeability of sediments, the rate of the water flow is smaller than the deposition rate, the pore pressure increases, which results in a lesser degree of compaction.

The material of the first type has sufficiently low permeability to impede the water flow so that there is a pore pressure buildup, which results in the pore pressure growing in excess of the hydrostatic values at the corresponding depths. On the other hand, the permeability of the material of the second type is high enough for the rate of the water flow to match the deposition rate. In the basin containing the material of the second type alone, there would be no pressure buildup and the pore pressure would be equal to the hydrostatic pressure at all depths. We can observe that the lines for the pore pressure and the hydrostatic pressure are parallel at the depths corresponding to the material of the second type, i.e., the pore pressure does not additionally grow in excess of the corresponding hydrostatic values, the difference is constant and is due to being trapped by the material of the first type from above.

It can also be seen that because of the increase of the pore pressure in the layers with the material of the first type, the

**Fig. 8** Pressures along a mesh column at  $t = 20$  Ma for the coarser and the finer meshes



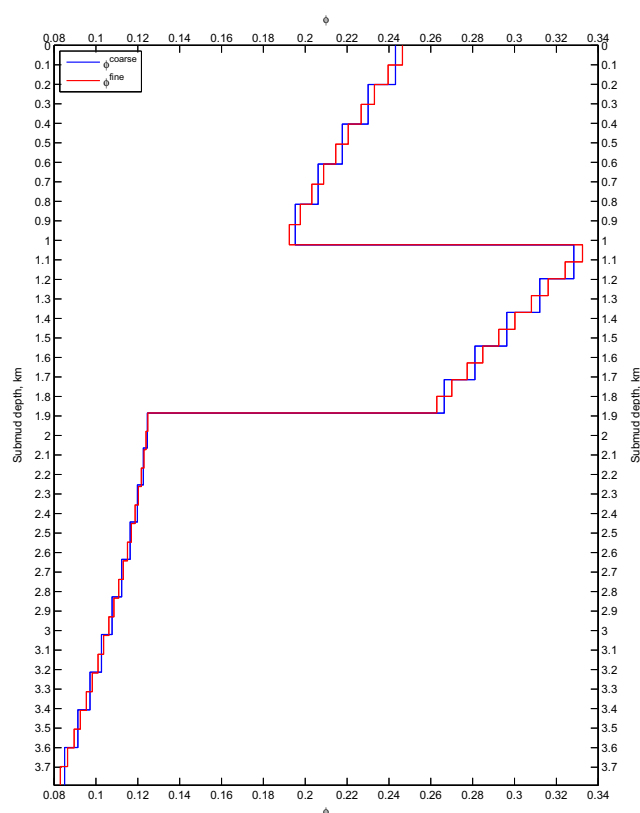


**Fig. 9** Porosities along a mesh column at  $t = 20$  Ma for the coarser and the finer meshes

basin at the end of the simulation is not yet fully compacted. If the deposition were to stop, after some time, the pore pressure would decrease to the corresponding hydrostatic values due to the water flow, and the depth of the basin would also decrease to the present day values.

It is worth noting that the geometry of the basin has been accurately resolved, which includes thin cells on the right in the pinchout geological layer. We also obtained expected distributions of pressures and porosities and were able to observe that the effects of the competing rates of the water flow and sedimentation were captured during the simulation. The simulation also suggests that for the provided estimates of the final values of porosities, a certain period without further sedimentation is required for the pore pressure to become hydrostatic and for the basin to assume the final geometry.

The proposed approach can be extended for the case of 3D basins with vertical compaction. With proper adjustments to the used sedimentation model, in particular with new conditions on coupling of the strictly vertical compaction and the 3D fluid flow, the presented algorithm and its implementation can be modified to support the extended model.

**Acknowledgments** We would like to thank Dr. Adam Singer for the helpful discussions. We would like to thank ExxonMobil management for permission to publish this paper.

## References

1. Audet, D., Fowler, A.: A mathematical model for compaction in sedimentary basins. *Geophys. J. Internat.* **110**, 577–590 (1992)
2. Barbeiro, S., Wheeler, M.F.: A priori error estimates for the numerical solution of a coupled geomechanics and reservoir flow model with stress-dependent permeability. *Comput. Geosci.* **14**, 755–768 (2010)
3. Brezzi, F., Fortin, M.: Mixed and hybrid finite element methods. Springer, Heidelberg (1991)
4. Chen, Zh., Ewing, R.E., Lub, H., Lyons, S.L., Maliassov, S., Ray, M.B., Sun, T.: Integrated two-dimensional modeling of fluid flow and compaction in a sedimentary basin. *Comput. Geosci.* **6**, 545–564 (2002)
5. Davis, T.A.: Direct methods for sparse linear systems. SIAM (2006)
6. Hantschel, T., Kauerauf, A.I.: Fundamentals of basin and petroleum systems modeling. Springer, Heidelberg (2009)
7. Kuznetsov, Yu.A.: Mixed finite element methods on polyhedral meshes for diffusion equations. In: Glowinski, R., Neittaanmäki, P. (eds.) Partial differential equations: modelling and numerical simulation, pp. 27–42. Springer, The Netherlands (2008)
8. Kuznetsov, Yu.: Approximations with piece-wise constant fluxes for diffusion equations. *J. Numer. Math.* **19**(4), 309–328 (2011)
9. Boyarkin, O., Kikinzon, E., Kuznetsov, Yu., Prokopenko, A.: Approximations with piece-wise constant fluxes for diffusion equations on polyhedral meshes: algorithms and applications. *Russian J. Numer. Anal. Math. Model.* **27**(4), 339–368 (2012)
10. Kim, J., Tchalepi, H.A., Juanes, R.: Stability, accuracy and efficiency of sequential methods for coupled flow and geomechanics. *SPE Int. SPE* **119084**, 1–19 (2009)
11. Mikelić, A., Wheeler, M.F.: Convergence of iterative coupling for coupled flow and geomechanics. *Comput. Geosci.* **17**, 455–461 (2013)
12. Roberts, J.E., Thomas, J.-M.: Mixed and hybrid method. In: Ciarlet, P., Lions, J. (eds.) Handbook of numerical analysis, Vol. II, pp. 523–639. North Holland, Amsterdam (1991)
13. Samier, P., De Gennaro, S.: Iterative coupling of geomechanics with reservoir simulation. *SPE Reservoir Simulation Symposium*, Houston, TX USA (2007)
14. Settari, A., Maurits, F.: Coupled reservoir and geomechanical simulation system. *SPE J.* **3**, 219–226 (1998)
15. Sørensen, J.: Formulation and application of element methods in the simulation of pressure and temperature history of geological basins. *Int. J. Numer. Anal. Meth. Geomech.* **13**, 525–543 (1989)
16. Wangen, M.: Vertical migration of hydrocarbons modelled with fractional flow theory. *Geophys. J. Int.* **115**, 109–131 (1993)
17. Wangen, M.: A finite element formulation in Lagrangian coordinates for heat and fluid flow in compacting sedimentary basins. *Int. J. Numer. Anal. Meth. Geomech.* **17**, 401–432 (1993)
18. Wangen, M.: Two-phase oil migration in compacting sedimentary basins modelled by the finite element method. *Int. J. Numer. Anal. Meth. Geomech.* **21**, 91–120 (1997)
19. Wheeler, M.F., Xue, G., Yotov, I.: Coupling multipoint flux mixed finite element methods with continuous Galerkin methods for poroelasticity. *Comput. Geosci.* **18**, 57–75 (2014)